Green and scalable preparation of highly conductive alkali metal-dhta coordination polymers

Toni Grgurić,†[a] Marta Razum,†[a] Valentina Martinez,†[a] Goran Zgrablić,*[b] Ana Senkić,[b] Bahar Karadeniz,[a] Martin Etter,[c] Ivana Brekalo,[a] Mihails Arhangelskis,[d] Luka Pavić,*[a] Krunoslav Užarević*[a]

[a]Ruder Bošković Institute, Bijenička c. 54, 10000 Zagreb, Croatia

[b]Institute of Physics, Bijenička c. 46, 10000 Zagreb, Croatia

[c]Deutsches Elektronen-Synchrotron (DESY), Notkestr. 85, 22607 Hamburg, Germany

[d]Faculty of Chemistry, University of Warsaw, 1 Pasteura Street, 02-093 Warsaw, Poland

KEYWORDS mechanochemistry, electric conductivity, alkali CPs

ABSTRACT: 2,5-dihydroxyterephthalic acid (H_4**dhta**) is well-known for its use in the construction of functional metal-organic frameworks (MOFs). Among them, simple coordination polymers (CPs), such as lithium and sodium coordination polymers with H_4**dhta**, have been used successfully to synthesize electrically conductive MOFs and have also demonstrated great potential as positive or negative electrode materials on their own. However, there has been little exploration of the structure and physicochemical properties of these and other alkali complexes of H_4**dhta**. To address this gap, a series of 1:1 alkali metal-**dhta** coordination polymers (Li-, Na-, K-, Rb-, Cs-), showing high conductivity with a non-monotone trend inside the series, were synthesized using green mechanochemical processing. The crystal structures of these metal-organic conductors reveal the rich coordination chemistry of the alkali cations ranging from four to ten. Their electric conductivity was influenced by cation type, coordination environment, the water present in the structure, atmosphere, and temperature. Overall, this study not only sheds light on the fascinating behavior and efficiency of monoalkali metal-dhta CPs and paves the way for the development of more efficient coordination materials for energy storage and conversion applications but also proves that sometimes the smallest changes in materials' structure and composition can make a significant difference in conductivity.

Introduction

With the growing energy demands of modern society, there is a constant search for new materials for energy generation and storage. Metal-organic frameworks (MOFs), coordination polymers built from metal cations and organic linkers, are now an important topic in material science due to their porosity, modularity, and facile engineering of their structure and properties by choice of the metal node or the bridging ligand.[1–5] However, MOFs have some inherent limitations for electrical applications. Their porosity and the bonding between the ligand and metal center, in many cases, lead to large energy gaps and semiconducting or insulating properties. Despite this fact, electrically conductive coordination polymers have attracted attention in the fields of electrocatalysis, sensing, and energy storage, as well as their potential to stabilize topologically interesting electronic structures.[6–15] Strategies for increasing the conductivity of these porous conductors are based primarily on improving the metal-ligand bonding (through-bond approach) and non-covalent interactions between the organic ligands (through-space approach) or on including guests in the pores to ensure continuous and strong charge transport pathways. Several excellent reviews are now available on conducting MOFs, describing these strategies and different MOF families in detail. [16–18]

A particularly interesting family of conductive MOFs is based on 2,5-dihydroxyterephthalic acid (or 2,5-dioxido-1,4-benzenedicarboxylate, H_4**dhta**), a ditopic chelating quinone ligand best known for building the MOF-74 (CPO-27) family.[19] These MOFs, built from H_4**dhta** and several different divalent metal cations, are widely investigated for their stability, high porosity, interesting magnetic properties, and high potential for catalysis.[20–23] The application potential can be further expanded by introducing heterometals in the framework, which can be controllably achieved by mechanochemistry. This fast, scalable, and sustainable synthetic technique relies on mechanical energy input to initiate a chemical reaction.[24–26] MOF-74 compounds are characterized by infinite 1D oxometallic chains along the crystallographic *c*-

axis, where the cations are close and bound by oxygen bridges, so they were a natural target of several studies for their electrical conductivity. It was discovered that the through-bond pathways achieved through the 1D chain result in low conductivity in MOF-74 materials,[27] in the range of 10^{-14} to 10^{-13} S/cm. The conductivity, however, can be manipulated by the coordinated solvent molecule or protic guest cations and increased by replacing oxygen in the oxometallic chain with softer electron-rich thiol groups; thus, increasing orbital overlap with the relatively soft metal cations usually used to build MOF-74.[28–31]
Recently, a novel approach has emerged where the hard oxo-anions (such as **dhta**) can be well matched with hard alkali anions, providing better orbital overlap and better through-bond electron transfer. Due to their electronic and redox properties, such coordination polymers of H_4**dhta** recently showed promise for developing hybrid alkali metal-organic positive or negative electrode materials. Bimetallic Li-Mn-**dhta** MOF proved to be one of the few rare and efficient Li-reservoir positive electrodes where the electrochemical performance could be controlled through ligand to metal stoichiometry and changes in the topology of the secondary building unit of MOF.[32] Even simpler coordination polymers not involving transition metals, such as lithium salts of H_4**dhta**, showed remarkable capability as either anodes or cathodes in Li-ion batteries, with excellent cyclability even in a symmetric battery setup.[33,34] Based on these results, it is evident that alkali metal-**dhta** materials may be a strong addition to the field. It is thus surprising that the structural and physicochemical chemistry of alkali metal coordination polymers of H_4**dhta** is almost entirely neglected.[35]
Here, we present a comprehensive synthetic, structural, and conductivity study of H_4**dhta** and a series of 1:1 alkali metal-**dhta** compounds (Li-, Na-, K-, Rb-, Cs-) prepared by mechanochemistry. Compared to solution syntheses of these materials, mechanochemical synthetic processes allowed for stoichiometry control and proved beneficial regarding time, yield, and reduced waste. The course of mechanochemical reactions was monitored in real-time by high-energy synchrotron X-ray diffraction[36] to establish their kinetic and mechanistic parameters and enable optimization for large-scale production. Based on the insights obtained, we subsequently conducted preliminary scale-up experiments of **Na-dhta** and **K-dhta**. The crystal structures, resolved for all of the alkali-**dhta** compounds, reveal them to be coordination polymers with a rich cation coordination chemistry, varying in their coordination number between four, six, seven, eight, and ten (**Fig. 1**).

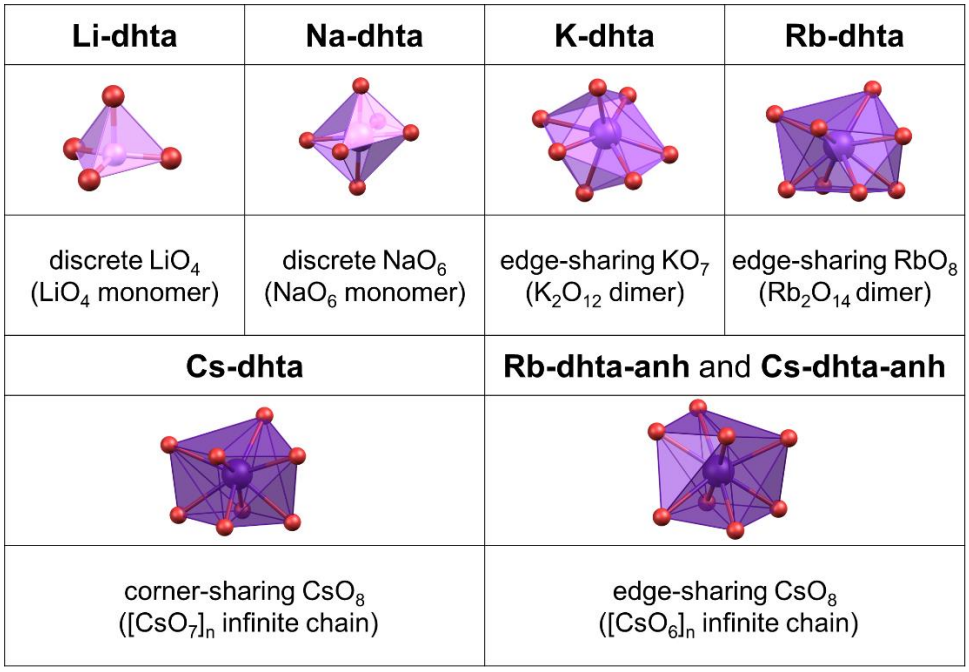

Figure 1 Coordination polyhedra of M_{alk} ions and the forms in which they appear in M_{alk}-**dhta** (M_{alk} = Li, Na, K, Rb, Cs) compounds

Water is present in most of the investigated compounds and plays a crucial role in not only filling the coordination sphere of alkali cations and bridging the larger cations into dimers or polymers but also in their physico-chemical properties. At elevated temperatures, these compounds lose the coordinated water, leading to changes in structure and the coordination environment of the metal, as established by diffraction studies and Raman spectroscopy. The impedance spectroscopy reveals unexpectedly high conductivity for all target compounds, including the highest reported among lithium-**dhta** materials. Among the studied alkali-**dhta** compounds, we observe a non-monotonic trend in DC conductivity as a function of the coordination sphere, increased complexity of polyhedron arrangements, and a strong influence of atmosphere and temperature on their electrical properties. [37]

Experimental

Both the conventional laboratory ball-milling for mechanochemical preparations of **Li-dhta**, **Na-dhta**, **K-dhta, Rb-dhta**, and **Cs-dhta** and in-situ experiments were performed at 30 Hz in identical 14 mL PMMA jars using two 1.6 g (7 mm) ZrO_2 balls, and the exact amounts of starting materials without solvent additive, with milling duration of 30 minutes. The procedure involved milling 300 mg (1.514 mmol) of H_4**dhta** with 36.3 mg (1.514 mmol) of LiOH, 60.6 mg (1.514 mmol) of NaOH, 84.9 mg (1.514 mmol) of KOH, 198.9 mg (1.514 mmol) of $RbOH{\cdot}H_2O$ or 254.3 mg (1.514 mmol) of $CsOH{\cdot}H_2O$, respectively. The powders obtained from the process had colors ranging from yellow to beige. The milling products were also subjected to accelerated aging[38] in H_2O (at 45°C and relative humidity (RH) of 98%) to study their moisture stability and enhance their crystallinity. Scale-up milling experiments for the synthesis of **Na-dhta** and **K-dhta** were conducted at scales three times and fifteen times greater than the initial experiments, using a mixer mill or planetary mill, respectively. (details in the SI, Section 2.13)

Solution crystallizations were performed to determine whether mechanochemical and solution syntheses afford the same products and to obtain single crystals of the ball-milling products. The 1:1 molar ratio of 2,5-dihydroxyterephtalic acid (H_4**dhta**) and the corresponding alkaline hydroxide used in ball milling was also used for the solution syntheses to enable direct comparison. Due to the poor water solubility of H_4**dhta**, solution syntheses were performed using a mixture of ethanol and water. In all cases, the conversion and yields were almost quantitative, but in several solution syntheses, a small portion of pure H_4dhta crystallized together with the **M_{alk}-dhta** CPs.

To obtain crystals of **Li-dhta** and **Na-dhta,** 40 mg (0.202 mmol) H_4**dhta** was dissolved in 6 mL of ethanol and mixed with 4.8 mg (0.202 mmol) of LiOH or 8.1 mg (0.202 mmol) of NaOH, respectively, each dissolved in 2 mL of deionized water.

For **K-dhta**, **Rb-dhta,** and **Cs-dhta,** 20 mg (0.101 mmol) H_4**dhta** was dissolved in 3 mL of ethanol and mixed with 5.7 mg (0.101 mmol) of KOH, 13.3 mg (0.101 mmol) of $RbOH{\cdot}H_2O$ or 17 mg (0.101 mmol) of $CsOH{\cdot}H_2O$, respectively, each dissolved in 1 mL of deionized water.

The solutions were homogenized by an ultrasonic bath and evaporated slowly at room temperature (~ 25 °C). After a few days, orange-yellow prism-shaped crystals were obtained for **Li-dhta** and **Na-dhta**, yellow prism-shaped crystals for **K-dhta**, and light-yellow needle-shaped crystals for **Rb-dhta** and **Cs-dhta**, all suitable for single crystal X-ray diffraction (SC-XRD). Interestingly, in some of the crystallization attempts, needle-like yellow crystals of anhydrous H_4**dhta** were observed, the crystal structure of which has not yet been reported**.**

All the products were characterized by powder X-ray diffraction (PXRD), infrared spectroscopy (IR), Raman spectroscopy, and thermogravimetric analysis (TGA). Impedance spectroscopy (IS) measurements at ambient temperature in air and inert dry conditions (LN_2 atmosphere) and at elevated temperatures under LN_2 flow were performed on pellets of **M_{alk}-dhta** samples prepared by ball milling to investigate their electrical properties. Furthermore, EDAX-SEM analysis, in combination with PXRD analysis, was conducted on the pressed samples to assess the impact of the pelletization process on the material's structure, particle size, and particle clustering.

The anhydrous phases of the **M_{alk}-dhta** compounds were prepared by heating them in the TGA instrument to 200°C at a heating rate of 1°C min^{-1} under a nitrogen flow. The structure of **Cs-dhta-anh** and **Rb-dhta-anh** were determined from PXRD data and confirmed through periodic DFT calculations. Full experimental details and analyses can be found in the SI.

Results and discussion

Structural characterization

The solution syntheses resulted in crystalline **M_{alk}-dhta** products with crystallites of suitable size for SC-XRD studies. All the crystal structures are described in detail in the SI, and their brief description is given here for easier comprehension of the manuscript.

Despite being commercially available and important in MOF chemistry for decades, the crystal structure of pure H_4**dhta** has not been reported to date.[39] This issue may be attributed to the characteristic small, needle-like, and often fused crystals that precipitate from their solutions. Therefore, it is not unexpected that recent efforts have been directed toward elucidating the structure through powder diffraction techniques.[40] Fortunately, in some experiments, we observed bright-yellow crystals of H_4**dhta** occurring concomitantly with the **M_{alk}-dhta** product and solved the structure by SC-XRD. (**Fig. S2**) The crystal structure consists of planar sheets of hydrogen-bonded H_4**dhta** molecules that stack in the third dimension through π-π interactions (**Fig. S8**). The sheets are built from H_4**dhta** molecules forming chains of hydrogen-bonded carboxylic acid dimers, which are then hydrogen-bonded into layers through adjacent hydroxyl groups (**Fig. 2a**). The chains in the layers are oriented in the same direction. The PXRD pattern of commercial H_4**dhta** and the one simulated from crystal structure closely match **(Fig. S14).**

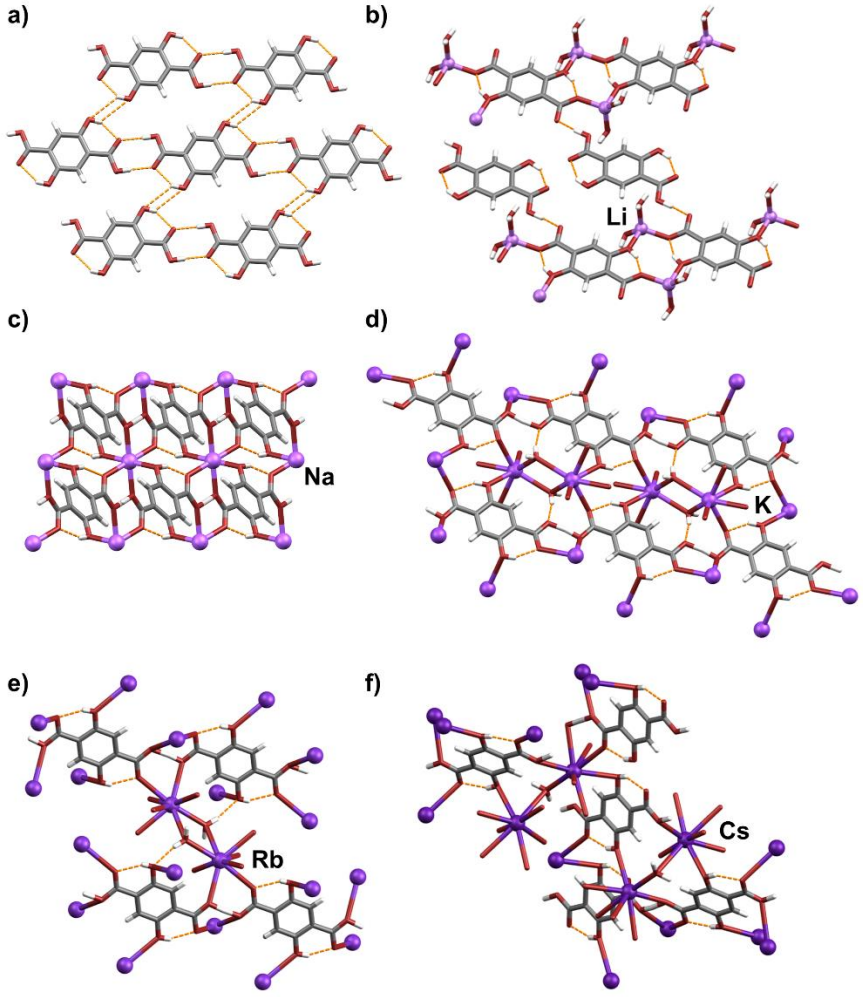

Figure 2 The simplified representation of the structures of H_4**dhta** (a) and **M_{alk}-dhta** CPs (M_{alk} = Li, Na, K, Rb, Cs) (b-f) showing the proximate environment around the alkali cation. For more details on the 3D structure of these alkali CPs, please see SI. Hydrogen bonds within the structures are displayed as orange dashed lines. Color code: M, purple; O, red; C, grey; H, white.

SC-XRD analysis further revealed that all the **M_{alk}-dhta** compounds are densely packed coordination polymers, with **Li-dhta** being a 1D coordination polymer, whereas all the others are 3D frameworks. While the overall metal-to-ligand molar ratio is 1:1 in all compounds, the alkali metal coordination numbers and metal-ligand connectivity increase with the size of the alkali cation (**Fig. 1, Fig. 2.b-f, Fig. S3-S7**). The lithium- and sodium-based 3D coordination frameworks are built from LiO_4 and NaO_6 monomeric Secondary Building Units (SBUs) bridged through H_3**dhta**$^-$ anions, while the potassium- and rubidium-based frameworks are formed by K_2O_{12} and Rb_2O_{14} dimer SBUs. In the dimers, two water molecules bridge the edge-sharing KO_7 and RbO_8 polyhedra, respectively, while H_3**dhta**$^-$ anions connect different dimers, forming the 3D scaffold. Cesium, on the other hand, produces infinite $[CsO_7]_n$ chains comprising corner-sharing CsO_8 polyhedra through single water molecule bridges. The chains form covalent bilayers through pendant H_3**dhta**$^-$ molecules, which are again stacked through Cs-H_3**dhta**$^-$ covalent bonds in the third dimension. In the case of lithium, the product is a 2:1 (Li:H_2**dhta**$^{2-}$) 1D coordination polymer cocrystallised with H_4**dhta** molecules, giving an overall 1:1 metal-to-ligand molar ratio (Li^+:H_4**dhta**:H_2**dhta**$^{2-}$ = 2:1:1; **Fig. S3**). The cocrystallised H_4**dhta** connects Li_2-H_2**dhta** chains oriented along the *b*- crystallographic axis through O–H···O hydrogen bonds into 2D supramolecular sheets, which are then stacked through an extensive network of H_2O-H_2**dhta**$^{2-}$ hydrogen bonds. In the other **M_{alk}-dhta** compounds, H_4**dhta** exclusively coordinates to the alkali metal, building complex coordinative 3D structures, making **Li-dhta** a notable exception in the series. In all cases, except for **Na-dhta,** which crystallizes without water, it was observed that the coordinated water serves to enhance the structure *via* hydrogen bonding or by acting as a bridging ligand between two alkali metals in the dimers mentioned above and chains. These water molecules arise from either the acid-base neutralization reaction of H_4dhta and the corresponding M_{alk} hydroxide or are liberated from the M_{alk} hydroxide hydrates during decomposition preceding this neutralization. Upon heat-induced dehydration of **Cs-dhta** polymer, $[CsO_7]_n$ chains transform into $[CsO_6]_n$ chains comprised of edge-sharing CsO_8 polyhedra. Analogously, the **Rb-dhta** dimers transform into $[RbO_6]_n$ chains comprised of edge-sharing RbO_8 polyhedra. The two dehydrated compounds are isostructural, and their structure will be described in more detail in the "Thermal behavior study" section.

The FTIR spectra of the synthesized compounds exhibit similar characteristics. (**Fig. S17, S20, S23, S25, S27**). Notably, they display stretching vibration modes of the C–O bond of the carboxylic group of the ligand at approximately 1636 cm^{-1}. The absorption peaks in the range of 1500 to 1300 cm^{-1} and 900 to 800 cm^{-1} correspond to the stretching vibration of the C=C bond and C-H in the aromatic ring, respectively. Furthermore, the peaks around 500 cm^{-1} (fingerprint region) are associated with alkali metal-oxygen bonds.

Judging by FTIR and PXRD analysis, the products are phase pure, and PXRD patterns of crystallization products (bulk sample and calculated from SCXRD data) match those of the microcrystalline mechanochemical products, showing that coordination mode and packing can efficiently translate from solution to ball milling (**Fig S15, S19, S22, S24, S26**). Of the two synthetic methods used, mechanochemistry is faster (<30 min vs. 2-3 days for crystallization from solution) and requires no solvents or purification. In both synthetic approaches, the yield is comparable (quantitative conversion), but in solution syntheses, H_4dhta often crystallizes concomitantly with alkali-dhta products.

Real-time *in situ* monitoring of mechanochemical reactions

Several real-time *in-situ* PXRD monitoring experiments were conducted at the Deutsches Elektronen-Synchrotron (DESY) to gain insight into reaction mechanisms and to see if the sustainability of mechanochemical **M_{alk}-dhta** syntheses can be further improved by shortening reaction times. The monitoring details are described in SI in Section 1.6.

Owing to the complex reaction mixture rheology, we could not monitor the synthesis of **Li-dhta** using the *in-situ* technique, even after several attempts. Since the lithium-**dhta** compounds are of immense interest from an application standpoint, we have decided to monitor the reaction *ex-situ* using a benchtop diffractometer. This involved extracting a small amount of powder from the milled reaction mixture at 1-minute intervals. We can observe that the reaction starts during the first minute of milling and that as it progresses, the crystallinity of the product improves. (**Fig. S18**)

Immediately upon commencing the milling of NaOH with H_4**dhta**, an intermediate phase is visible in the reaction mixture, leading to the known hydrated phase of **Na-dhta-H_2O** product ($[Na(H_3dhta)(H_2O)_2]$)[39]

(**Fig. 3.a**) and finally to **Na-dhta**. Judging by the diffraction peaks of H_4**dhta** that are still present when the intermediate appears, the intermediate phase could be a metal complex with a higher metal-to-**dhta** ratio. The *ex-situ* experiments (**Fig. S21**), where H_4**dhta** and NaOH were milled together in several molar ratios, show a very similar pattern in Na:H_4**dhta** 3:1 and 4:1 complex, but structure solution from PXRD was not possible due to the inability to isolate the pure intermediate. This intermediate phase transforms quickly into the hydrated phase **Na-dhta-H_2O** ([Na(H_3dhta)(H_2O)$_2$]) after 15 minutes of milling, and the phase composition remains stable until the end of the experiment. The final product, analyzed upon the opening of the jar, corresponds well to the anhydrous Na-**dhta** phase obtained in the laboratory. The transformation from the hydrated to the dehydrated phase occurs immediately due to the tiny amount of byproduct water present.

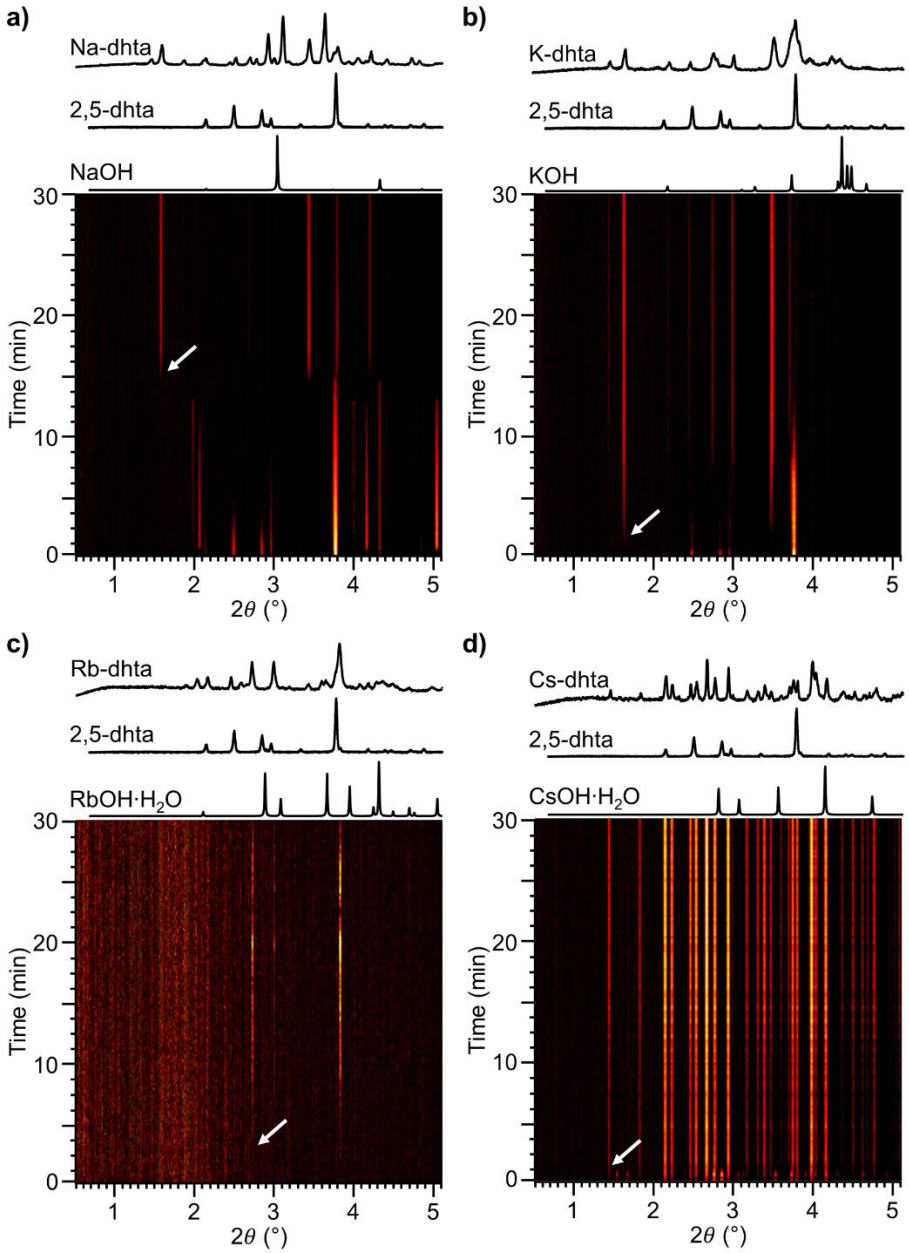

Figure 3 Time-resolved diffractograms from the *in situ* and real-time monitoring of the synthesis of (a) **Na-dhta** (b) **K-dhta** (c) **Rb-dhta** (d) **Cs-dhta**. Simulated diffraction patterns of referent **M_{alk}-dhta**, H_4**dhta**, and alkali hydroxides are given at the top. White arrows show the beginning of **M_{alk}-dhta** formation. X-ray beam: E ≈ 60 keV, λ = 0.20735 Å.

The reflections of KOH and H_4**dhta** start to disappear within 2 min from the start of milling and disappear entirely after 12 min, accompanied by the rise in intensity of the **K-dhta** reflections. (**Fig. 3.b**) No changes

in the intensities of the product were detected by the end of the milling experiment. Unlike for **Na-dhta**, the mechanochemical synthesis of **K-dhta** has no detectable intermediates.
The monitoring of **Rb-dhta** formation faced similar issues to that of **Li-dhta**, where the sticking of the reaction mixture to the wall of the vessel resulted in lower-quality monitoring data. However, we were able to observe that the reaction begins during the second minute of milling, after which there are no visible changes in the **Rb-dhta** diffraction intensities. The PXRD patterns also show no remaining $RbOH{\cdot}H_2O$ or H_4**dhta** peaks, implying that the reaction finishes almost immediately. (**Fig. 3.c**)
The Bragg reflections corresponding to **Cs-dhta** diffraction peaks were detected during the second minute of milling when the reflections of $CsOH{\cdot}H_2O$ and H_4**dhta** almost completely disappeared. The reflection intensities do not change until the end of the experiment. (**Fig. 3.d**)
To summarize, all mechanochemical $\mathbf{M_{alk}}$**-dhta** formations by dry milling are finished in minutes. Most of the monitored reactions proceed directly from the starting compounds to the products, with the only exemption being **Na-dhta**, where an intermediate (likely with a higher Na:**dhta** ratio) appears immediately upon grinding but reacts quickly with the remaining H_4**dhta** to form the 1:1 **Na-dhta** product. In all cases, the products are phase-pure and correspond to the $\mathbf{M_{alk}}$ **-dhta** compounds prepared by milling or from solution in the laboratory. Based on these insights, we designed the scale-up experiments on one-gram and five-gram scales for two chosen systems: **Na-dhta** and **K-dhta**. The one-gram syntheses were performed in a mixer mill and provided products identical to small-scale syntheses. Five-gram scale was performed in a planetary mill, where in the case of **Na-dhta,** a portion of **Na-dhta-H_2O** was observed, which readily transformed into **Na-dhta** by short exposure to heat. **K-dhta** was obtained pure on a five-gram scale, without traces of any polluting forms. No work-up was needed in all of these syntheses.

Thermal behavior studies

The thermal behavior of each compound was investigated by thermogravimetric analysis (TGA). The first step in each TG curve (at temperatures between 126 and 173 °C) indicates the loss of coordinated water molecules, except for **Na-dhta**, which is initially in the dehydrated form. (**Fig. S29.a-e**) Heating-induced dehydration is evidenced by the absence of the water O-H stretching bands at 3570 and 3500 cm^{-1} in the FTIR spectra (**Fig. S17, S20, S23, S25, S27**). This coordinated water can be distinguished from the water adsorbed to the surface or in defects during accelerated aging, as the latter is characterized by a broad band at approximately 3400 cm^{-1}. No other significant heating-induced changes were observed in the spectra. However, some bands exhibited broadening or shifting depending on the water content and slight changes in fingerprint area, probably due to the changes in M_{alk}-O bonds. The **Li-dhta** compound is distinguishable due to the presence of H_4**dhta** in its structure, rendering its spectra distinct from those of the other four compounds, which resemble one another.(**Fig. S17**). The dehydrated phases are stable until about 300 °C (**Fig. S29.a-e**) and exhibit significant structural changes compared to the original compounds. (**Fig. S28.f**) Complete compound degradation occurs at temperatures above 300 °C (~300-500 °C).
The structures of the anhydrous Cs-**dhta** (Cs-**dhta**-anh) and the anhydrous Rb-dhta (Rb-**dhta**-anh) were obtained by structure solution and refinement from capillary PXRD data (details in SI sections 1.8. and 2.9.) and confirmed through periodic DFT calculations (SI section 2.10.). The compounds are isostructural, and their structures conserve the 1:1 metal-to-ligand molar ratio found in the parent hydrated CPs and the single deprotonation of the H_3**dhta**$^-$ ligand. However, while each cesium ion in the hydrated CP was coordinated by two water molecules and six H_3**dhta**$^-$ ligands, the dehydrated CP is coordinated only by eight different H_3**dhta**$^-$ ligands. This results in infinite $[CsO_6]_n$ chains comprised of edge-sharing CsO_8 polyhedra (compared to $[CsO_7]_n$ chains comprised of corner-sharing CsO_8 polyhedra in the parent coordination polymer), Figure 1. Even more strikingly, the rubidium structure transforms from water molecule-bridged Rb dimers into the analogous infinite $[RbO_6]_n$ chains comprised of edge-sharing RbO_8 polyhedra. In both structures, two more hydroxyl oxygen atoms from already coordinated H_3**dhta**$^-$ molecules can be found at a distance of 3.712 Å and 3.799 Å for Cs and Rb, respectively. These distances are slightly larger than a typical Cs-O or Rb-O bond (**Fig. S32.a**) but significantly closer than the sum of Cs and O/Rb and O Van der Waals radii (4.95 and 4.55 Å, respectively). An argument could be made that these are infinite $[CsO_8]_n$ and $[RbO_8]_n$ chains comprised of edge-sharing CsO_{10} and RbO_{10} polyhedra, adding another dimension of structural variability to the prepared alkali **dhta** CPs. In both structures, the chains are connected through a complex network of π-π stacking and intermolecular

hydrogen bonds formed by the coordinated H_3**dhta**$^-$ ligands. Full structural details and description can be found in SI 2.8. We assume similar changes take place in other anhydrous **M$_{alk}$-dhta** compounds, but we were so far unable to obtain their crystal structures to confirm this.

To assess the influence of hydration in CP samples on the vibrational dynamics of frameworks, we measured Raman spectra for both dry and hydrated compounds in the low-frequency THz region (< 300 cm^{-1}) (**Fig. S36**), covering a range from 10 cm^{-1} to 1800 cm^{-1}. The THz region in vibrational spectra of CPs is particularly interesting because it encompasses intermolecular vibrations, i.e., low-frequency collective modes. [41] These can also be referred to as low-energy phonons (collective, quantized lattice vibrations) and are associated with the structural mechanics of CP materials, such as shearing, pore distortion, and breathing modes of the framework. [42–44] These low-frequency collective modes influence the fundamental properties of the framework, including adsorption, elasticity, structural transitions, instability, [44,45] and thermal conductivity.[46,47]

In the 400-1800 cm^{-1} region (**Fig. S36**), the organic linker modes dominate over other modes and exhibit characteristic frequencies resulting from typical functional groups that do not change significantly with the type of the incorporated metal atom into the structure. Thus, we base the assignment of our alkali metal-DHTA compounds on the mode assignments previously done for Zn-MOF-74[48] and Co-MOF-74.[49,50] We assigned the 805-812 cm^{-1} vibrations to the antisymmetric in-plane bending modes of the benzene ring β_{as}(COO−), 1280-1290 cm^{-1} vibrations to the C-O stretching mode ν(C−O) (the most intense mode) and the 1395-1415 cm^{-1} vibrations to the O-C-O symmetric stretching ν_s(COO−). We normalized the spectra of the dry and hydrated compounds to the intensity of the ν(C−O) mode, the most intense vibration in all studied compounds.

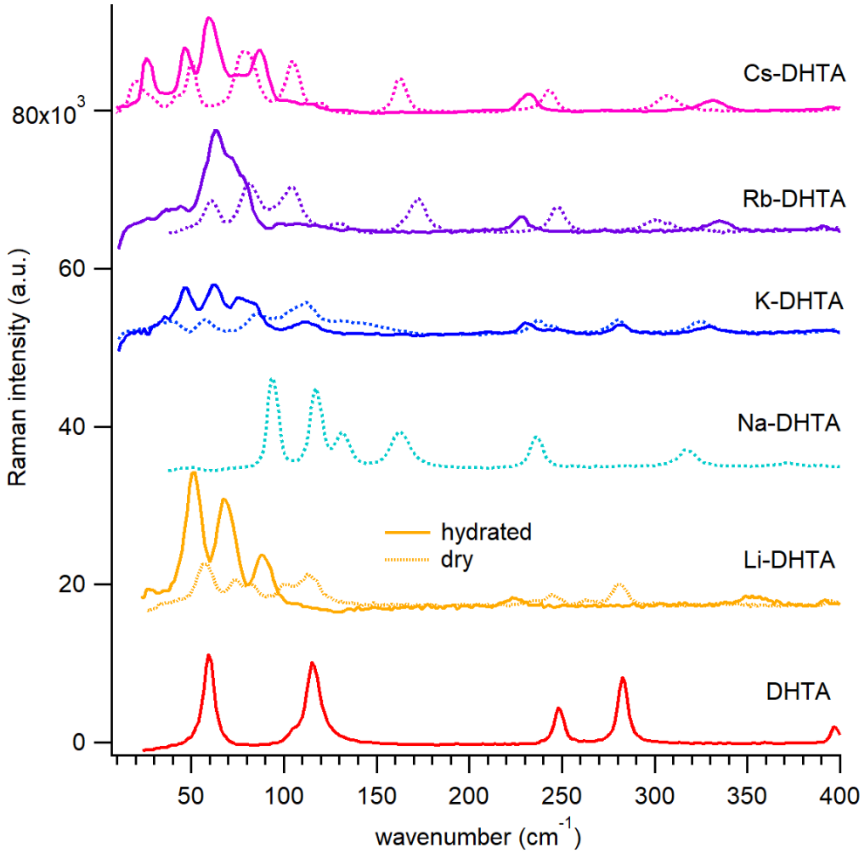

Figure 4 Low-wavenumber Raman spectra of H_4**dhta** and alkali metals-**dhta** compounds; dry (dashed lines) and hydrated (solid lines). The spectra of the dry and hydrated versions of a compound are normalized to the intensity of the ν(C−O) mode (for more details, please see SI).

This normalization allows us to observe how hydration strongly affects the low-frequency collective modes. As mentioned above, this part of the spectrum[51] is very sensitive to changes in crystal packing and electron structure in solids, so it is becoming extremely popular for distinguishing between polymorphic phases or even for detecting single atom replacements in the structure not possible to resolve by crystallographic methods.[52] However, these low-frequency resonances are delocalized among a large number of atoms in the crystal, making the assignment of a specific band not possible without employing advanced periodic density functional theory (DFT) calculations, so we will remain on a descriptive level.

Three to four modes, separated by 15-25 cm^{-1}, can be observed in hydrated Li-, Na-, K-, and Cs-**dhta** in the 10-120 cm^{-1} region (**Fig 4**), creating a comb-shaped spectrum with the lowest frequency mode at 20 cm^{-1} found in dry Cs-**dhta**. Interestingly, in Na-**dhta** (cyan dashed line), the intrinsically "dry" sample, modes with frequencies below 90 cm^{-1} are absent. In Rb-**dhta**, these modes are broader and overlap, with a maximum at 64 cm^{-1}, possibly indicating greater structural heterogeneity in this compound.

Dehydration leads to a couple of notable effects. The H_4dhta vibrations are clearly visible in dry Li-**dhta** compound, most likely due to the cocrystallised H_4dhta in the Li-**dhta** structure. These bands are not present in hydrated Li-**dhta**. Compared to the hydrated compounds (solid lines, **Fig. 4**), the low-frequency bands in dehydrated samples (dashed lines, **Fig. 4**) occur in higher wavenumber regions, and their overall intensity decreases. Specifically, in Li-**dhta**, the low-region spectrum intensity is three times weaker; in Rb-**dhta**, twice; and in Cs- and K-**dhta**, the intensity decreases by 25%. This indicates that low-frequency collective modes become less active upon dehydration of the alkali metal-**dhta** compounds, particularly for Li-**dhta**. Also, lower frequencies in the spectra (<70 cm^{-1}) gain more intensity at the expense of higher frequency ones (70-120 cm^{-1}), which is again most prominent in Li-**dhta**. However, as mentioned above, only combining these results with periodic DFT calculations can help to assign the physical motions to each observed peak[53] and provide insight into the mechanistic origin of the hydration-related changes in electrical conductivity in the presented alkali metals-**dhta** compounds.

Electrical properties

The electrical properties of H_4**dhta** and **M_{alk}-dhta** materials have been assessed by impedance spectroscopy on pellets prepared from powdered microcrystalline samples (see SI). As analyzed by PXRD and SEM, the **M_{alk}-dhta** materials are stable to the palletization process (SI). For the interpretation of the results of electrical characterization, it is crucial to correlate the observed features with the composition and structure of the samples to yield insight into the type of present charge carriers and their behavior within the material. There are several possible sources of electrical conductivity in these alkali coordination polymers. Firstly, the presence of coordinated water molecules and free carboxylic or phenol protons on the H_4**dhta** ligand is notable in all the studied **M_{alk}-dhta** samples, fostering an abundance of hydrogen (H)-bonds and thereby facilitating proton transport.[54,55] Secondly, delocalized electrons within the H_4**dhta** ligand should be considered, as they contribute to overall conductivity through bonding with the alkali metal and through space *via* π-π stacking. Thirdly, in addition to the intrinsic properties of the sample, one should acknowledge the potential presence of external (ambiental) water from the surrounding environment on the surface of the samples and in defects or interstitial spaces. This phenomenon directly influences proton conductivity and should be carefully accounted for during analysis.[54–57] Lastly, due to the coordination of alkali ions, their confinement, and decreased mobility, their ionic contribution to the overall conductivity is negligible, if any.

Figure 5.a illustrates the conductivity spectra for **M_{alk}-dhta** alongside pure H_4**dhta** ligand, measured at ambient conditions at T ~25 °C RH ~55%. The spectra show two distinct characteristics: *(i)* a distinct lower-frequency plateau, indicative of DC conductivity (frequency-independent part) related to the long-range movement of charge carriers, and *(ii)* a higher-frequency dispersion in conductivity (AC part) which originates from their localized movements.

Beyond these two observed spectral features, the spectra of all studied samples demonstrate a decrease in conductivity as frequency decreases in the low-frequency region. This phenomenon, recognized as electrode polarization (EP), arises from the accumulation of charge carriers at the gold electrodes. The increasing EP effect along the **K-dhta** - **Rb-dhta** - **Na-dhta** - **Cs-dhta** - **Li-dhta** series could indicate the increase in the number of available charge carriers for electrical transport along the series, likely linked to the structure of the studied samples. However, while the potential increasing number of charge carriers

could be connected to increasing conductivity, many other factors are also at play, as will be discussed later. Unlike the **M_{alk}-dhta** materials, pure H_4**dhta** displays a milder slope throughout the three regions and a less pronounced EP effect.

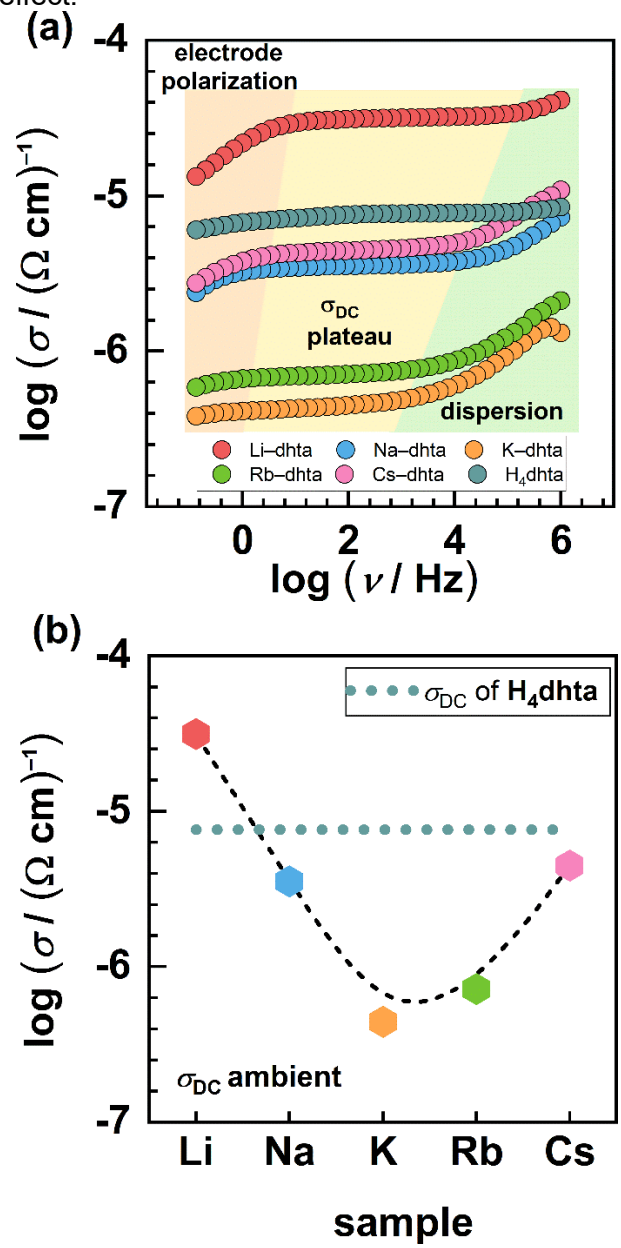

Figure 5 (a) Conductivity spectra and **(b)** trends of DC conductivity for all samples measured at ambient conditions (T ~25 °C and RH ~55%). In (b), each sample containing alkali ions is depicted by a data point, while the DC conductivity value for H_4**dhta** is denoted by a continuous teal dashed line. The graph line connecting points is only a guide for the eye.

Elaborating on electrical transport and the phenomenon of EP, impedance data is systematically presented using the Nyquist plot representation (see **Fig. S37**). Each spectrum consists of a high-frequency semicircle related to the bulk behavior and a low-frequency spur emanating from EP. One can see that H_4**dhta** lacks a full semicircle due to dispersion absence and features a long DC plateau across the frequency range. Throughout the samples, the evolution of the semicircular pattern closely mirrors the changes in conductivity. It becomes evident that as the conductivity decreases, the semicircular section increases while the corresponding EP spur becomes smaller, meaning a lower extent of mobile protons in the sample.

This EP effect indicates that protons are the primary charge carriers within all studied samples. Proton transport, a well-established phenomenon, occurs through proton hopping across a network of H-bonds within the sample. Generally, the interaction of external water molecules and the intrinsic proton carrier

sites in the structure contributes to the ease of electrical transport by forming a more intricate H-bonding network. This network serves as a pathway for the swiftest diffusion process and facilitates high proton conductivity. Water molecules, functioning as proton donors (i.e., tuning proton concentration) and carriers *via* H-bonds, significantly aid proton diffusion and act as mediators within the formed network. Therefore, H_2O plays a critical role in the capability of proton transfer.[31,54–56,58]. Examining the H_4**dhta** isotherm reveals a DC plateau "leaking" towards lower frequencies, particularly notable since it lacks crystalline water in the structure. It is, therefore, possible that in the case of H_4**dhta**, proton transfer has a slightly lower contribution to the overall conductivity, while through-space electron transfer facilitated by the extensive π-π stacking network in this quinone might play a more significant role.
On the other hand, the **Na-dhta** material similarly contains no coordinated water molecules. However, the EP effect here is more pronounced than in H_4**dhta**, possibly indicating a higher contribution of proton transfer to the overall conductivity. This is likely because the **Na-dhta** structure almost completely lacks π-π stacking, so the through-space electron transport is negligible, and the material conductivity relies on proton transfer, primarily influenced by ambient water. The beneficial effect of humidity seems to have a significant enough contribution that the overall conductivity is only slightly lower than in pure H_4**dhta**. The observed spectral features indicate the coexistence of all three contributions to overall conductivity (electron transfer, inherent proton transfer, and ambient water-enhanced proton transfer), with the dominance of proton conductivity and a pronounced effect of water under ambient conditions. The ambient water enhancement of overall conductivity is evident across all samples, especially in H_4**dhta** and **Na-dhta**, due to the absence of coordinated H_2O in their structures.

Table 1. DC conductivity measured at ambient conditions (T= 25 °C and 55% RH) and @150 °C in the cooling cycle, E_{DC} for the H-cycle before transformation and C-cycle.

Sample	σ_{DC}/(Ω cm)$^{-1}$ @25°C	Δ σ_{DC}/(Ω cm)$^{-1}$ @ 55% RH and 10 %RH	σ_{DC}/(Ω cm)$^{-1}$ @150°C	E_{DC} / eV in H-cycle	E_{DC} / eV in C-cycle
Li-dhta	$3.16\cdot10^{-5}$	~$1\cdot10^{-4}$	$2.95\cdot10^{-9}$	1.13	1.45
Na-dhta	$3.55\cdot10^{-6}$	~$2.0\cdot10^{-8}$	$9.33\cdot10^{-10}$	1.06	1.29
K-dhta	$4.47\cdot10^{-7}$	~$8.0\cdot10^{-4}$	$5.62\cdot10^{-10}$	0.56	1.20
Rb-dhta	$7.24\cdot10^{-7}$	~$2.0\cdot10^{-3}$	$1.15\cdot10^{-9}$	0.61	1.16
Cs-dhta	$4.45\cdot10^{-6}$	~$2.0\cdot10^{-7}$	$1.86\cdot10^{-10}$	0.99	1.15

As the size of the alkali cation increases, so does the coordination sphere, resulting in a variation in coordination number from four to even ten in the dehydrated sample (**Fig. 1**). The complexity of polyhedron arrangements grows with the increased coordination sphere, from monomeric SBUs over edge-sharing dimer SBUs to corner-sharing 1D chain SBUs. When the DC conductivity values obtained under ambient conditions are presented as a function of alkali ion radius (**Fig. 5.b** and **Table 1)**, a non-monotonic change in conductivity, characterized by a minimum in the **K-dhta** sample ($\sigma_{DC} = 4.43\cdot10^{-7}$ (Ω cm)$^{-1}$) is evident. The conductivity trend can be divided into three groups, differentiated by the different SBU polyhedron types. The first and most conductive group comprises samples with monomeric SBUs containing Li^+ and Na^+ cations. Notably, the sample exhibiting the highest conductivity is **Li-dhta**, with a DC conductivity value of $3.14\cdot10^{-5}$ (Ω cm)$^{-1}$, which is almost two orders of magnitude higher than both the best-performing MOF-74 family member[29] (Fe-MOF-74-DMF, $\sigma_{DC} = 3.2\cdot10^{-7}$ (Ω cm)$^{-1}$) and the best-reported lithium-dhta material[33] (tetralithium-**dhta**, $\sigma_{DC} = 1.1\cdot10^{-7}$ (Ω cm)$^{-1}$), which was tested for high-rate lithium batteries in the form of graphene composite. In comparison, the other monomeric SBU coordination polymer, **Na-dhta**, shows a marked decrease in conductivity of an order of magnitude ($\sigma_{DC} = 3.55\cdot10^{-6}$ (Ω cm)$^{-1}$). This can be attributed to two main factors: the differences in the coordination sphere and the presence of coordinated H_2O and cocrystallised H_4**dhta** in the **Li-dhta** sample. The coordinated water molecules in **Li-dhta** significantly enhance the proton-transfer capabilities of the sample. At the same time, the cocrystallised H_4**dhta** provides an extensive network of H-bonds that further enhances proton transfer and π-π stacking, which enhances an electron transfer contribution to the overall

conductivity. Despite the lack of coordinated H_2O in the **Na-dhta** sample, its conductivity remains relatively high, which will be commented on lower in the section dedicated to the dependence of conductivity on ambient conditions and RH. The conductivity significantly decreases when transitioning from monomeric to dimeric SBUs in **K-dhta** and **Rb-dhta**. The formation of edge-sharing dimers *via* coordinated water molecules aggravates charge transfer since it hinders the water molecules' mobility and, thus, their ability to enhance proton transfer. A comparison between **K-dhta** and **Rb-dhta** reveals a slightly higher conductivity value for the **Rb-dhta** sample ($4.43 \cdot 10^{-7}$ $(\Omega\ cm)^{-1}$ vs $7.18 \cdot 10^{-7}$ $(\Omega\ cm)^{-1}$), which may be attributed to the presence of stronger H-bonds. Finally, in the **Cs-dhta**, corner-sharing H_2O-Cs *zig-zag chains* are interconnected with both water- and **dhta**-based H-bonds, as well as π-π stacking of the **dhta** anions. Importantly, the infinite polymeric $[Cs\text{-}O]_n$ chain is not only covalently bound through the bridging water molecules, but each of those water molecules is also H-bonded to the closest H_3**dhta**$^-$ oxygen. This essentially creates an infinite 1D H-bonded chain intertwined with the polymeric $[Cs\text{-}O]_n$ chain (**Figure S32**), thus significantly enhancing proton transport and culminating in a DC conductivity value of $4.47 \cdot 10^{-6}$ $(\Omega\ cm)^{-1}$, an order of magnitude higher than the dimeric SBU **M_{alk}-dhta** materials, and even slightly higher than the monomeric SBU **Na-dhta**.

It is evident that structural variations - especially the presence of coordinated water - have a substantial effect on the DC conductivity and that proton conductivity is a large (if not the main) contributor to the overall electrical conductivity of these samples. Therefore, ambient water may play a crucial role in the surprisingly large DC conductivity values of **M_{alk}-dhta** coordination polymers. To estimate this contribution, we measured the conductivity spectra in a dry environment (LN_2) characterized by RH of ~10% % and cycled back to ambient conditions(**Fig. S38**). Unsurprisingly, the decrease in RH leads to a significant overall drop in the conductivity values of all samples. At RH ~10%, there is minimal possible interaction between external water molecules and coordinated water and ligand groups via hydrogen bonding. This leads to a decreased proton transport rate primarily confined to the surface region, resulting in diminished conductivity. The most pronounced impact is on the **Cs-dhta** and **Na-dhta** samples, where reductions of almost seven and eight orders of magnitude, respectively, were noted, **Table 1**. In **Na-dhta**, with no coordinated water, ambiental water significantly influences conductivity by actively contributing to proton donation and building proton pathways through H-bonds, so this significant difference is almost expected. To further rationalize the difference in conductivity for the **Cs-dhta** system and see if it might be related to dehydration, we exposed the parent material to a vacuum. The resulting material (**Fig. S28**) is identical to the one obtained by thermal dehydration (**Cs-dhta-anh**), strongly implying that the cause of this strong humidity dependence is the dehydration of the sample. A look at the structure of **Cs-dhta-anh** shows that while the infinite 1D covalent chain is preserved, the associated H-bonded chain in the parent structure is non-existent in **Cs-dhta-anh**. Since that infinite H-bond chain is likely the cause of such sizeable proton-transfer conductivity in the parent Cs-dhta material, it is unsurprising that its disappearance causes a significant drop in conductivity, leaving only through-bond electron transfer.[55,59,60] The noticeable dependence of conductivity on RH underscores that, in the studied samples, water molecules not only serve as a medium to modulate the concentration of protons by adsorbing on the surface of the sample but also actively participate in building a continuous hydrogen-bond network, facilitating effective proton conducting pathways. Notably, the significant difference in conductivity at different ambient humidity values and the possibility of successful cycling potentially make these materials promising candidates for water-sensing devices.

Seeing the extreme effect of ambient humidity on the conductivity of these materials, we also decided to study the influence of temperature. We conducted a series of temperature-dependent measurements for all samples. Initially, the samples underwent a heating cycle reaching 100 °C to eliminate adsorbed moisture. Subsequently, temperature cycles were planned based on TGA analysis (SI section 2.8.), resulting in a sequence of cycles including heating from 30 °C to 220 °C (H-Cycle) and cooling back to 30 °C (C-Cycle). The conductivity spectra exhibited an explicit temperature dependence, where increased temperature resulted in increased conductivity, consistent with the semiconductive behavior of known metal-**dhta** samples.[16,56] The DC conductivity demonstrated Arrhenius temperature dependence and has characteristic activation energy. The activation energy, E_{DC}, for each sample, and across both the heating and cooling cycle, was determined from the slope of $(\log(\sigma_{DC}))$ plotted against the reciprocal of temperature $(1000/T)$, using the Arrhenius equation: $\sigma_{DC} = \sigma_0 \exp(-E_{DC}/k_B T)$, where σ_{DC} is the DC conductivity, σ^*_0 is the pre-exponential factor, E_{DC} is the activation energy, k_B is the Boltzmann constant, and T is the temperature (K). The values of E_{DC} are reported in **Table 1**. Arrhenius plots for all

samples are presented below, showcasing heating and cooling cycles. These plots reveal distinct phase transformations occurring at specific temperatures, aligning well with TG measurements. Notably, the phase transitions are observed in the heating cycle, which reaches up to 220 °C, while no further transformations are observed during the subsequent cooling cycles to 30 °C.

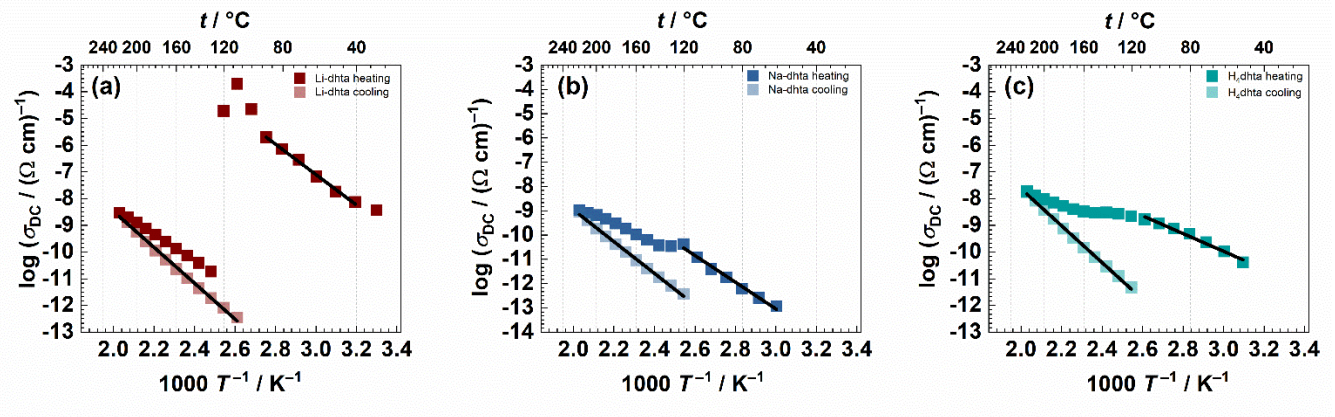

Figure 6 Arrhenius plot for the DC conductivity of (a) **Li-dhta**, (b) **Na-dhta**, (c) H_4**dhta**. At cooling temperatures below 120 °C, conductivity values are low, and the instrument limit of the IS setup we used and data are not shown.

For the **Li-dhta** sample, the initial dehydration process occurs within the temperature range of 100-120 °C (**Fig. 6.a)**, coinciding with the TGA-detected release of 2 coordinated water molecules. This effect is accompanied by a pronounced and sudden reduction in DC conductivity of 8 orders of magnitude. The loss of coordinated water leads to changes in the coordination structure of the compound, and after "stabilization," there is a further monotone increase in conductivity of the presumably dehydrated phase with an increase in temperature. A different pattern emerges with the **Na-dhta** sample (**Fig. 6.b)**. The detected change does not cause a sudden drop in DC conductivity, as observed in **Li-dhta**. Instead, a knee point manifests, with a discrete reduction in DC conductivity followed by a subsequent increase. Since the **Na-dhta** sample exhibited no changes on the TG curve until approximately 300 °C, the change cannot be rationalized by water loss and structural rearrangement process as above. To understand this behavior, we performed temperature-dependent measurements on the alkali-free H_4**dhta** sample (see **Fig. 6.c)**. One can notice similar spectra for the H_4**dhta** and **Na-dhta** samples, where the change occurs at 130 °C. This strongly suggests that the observed behavior for the **Na-dhta** sample is related to changes in the H_4**dhta** ligand.

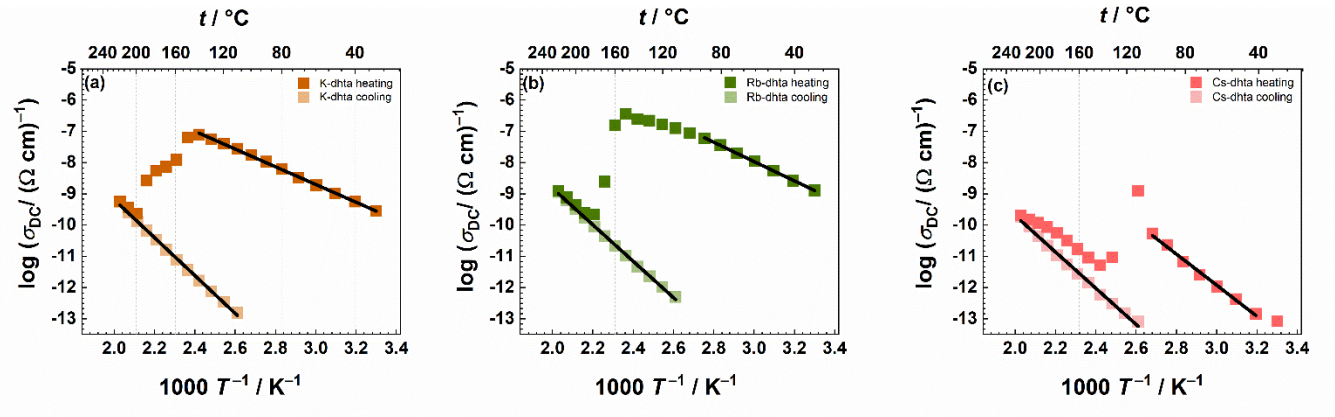

Figure 7 Arrhenius plot for (a) **K-dhta**, (b) **Rb-dhta** and (c) **Cs-dhta**. At cooling temperatures below 120 °C, conductivity values are low, and the instrument limit of the IS setup we used, and data are not shown

The other dimeric SBU polymer, **K-dhta**, exhibits a substantial decrease in DC conductivity upon the release of coordinated water by nearly three orders of magnitude. Unlike **Li-dhta**, this change is gradual rather than sudden, within the 130-150°C range (**Fig. 7.a**). In **K-dhta** dimers, two potassium cations are bridged by a coordinated water molecule into a dimer, resulting in strongly bound water molecules that are slower to release and, thus, a shift of dehydration temperature to higher values. Analogous behavior

is observed in the case of **Rb-dhta** (**Fig 7b**), which has a similarly high dehydration temperature due to tightly bound water in Rb-O-Rb dimeric SBUs. The Arrhenius plot for **Cs-dhta**, presented in **Figure 7.c**, reveals another rapid decrease in conductivity corresponding to the temperature of coordinated H_2O release at 110-130°C, akin to the behavior observed in the **Li-dhta** sample and analogous to the one observed when collecting **Cs-dhta** spectra at low humidity. This decline corresponds to a reduction of approximately four orders of magnitude but is significantly recovered upon heating to 220 °C. This recovery is likely due to the above-mentioned through-bond electron transfer. This type of conductivity enhancement in CPs is typically achieved by replacing hard N- or O-based ligands (amines, carboxylates, etc) with softer ligands (e.g., S-based thiols) to create better orbital overlap with the soft metals traditionally used in MOF synthesis (Fe, Ni, Mn, etc.). In our case, a similar effect is achieved by introducing a harder (but still softest of the alkali metals) metal to better match the hard O-based ligand. Overall, in the heating cycle for all samples, we observe specific modifications related to the release of coordinated water and changes in the H_4**dhta** ligand, resulting in significantly lower conductivities at 150 °C than ambient measurements (**Fig. 8.b**). It is important to note that while the effects of changes in the ligand are most pronounced in pure H_4**dhta** and the **Na-dhta** samples, they are likely also present in the other samples but seem to be masked by the much larger effects of coordinated water release. During the heating cycle, all hydrated samples show a sudden decline and non-monotonic change in DC conductivity due to H_2O release, while a consistent decrease in DC conductivity is observed in all samples during the cooling cycle (**Fig. 8.a)**. As for the activation energy, in the heating cycle, there is a non-monotonic trend (**Table 1**) in the range from 0.56-1.13 eV with a minimum for the sample **K-dhta** with an E_{DC} of 0.56 eV. On the other hand, in the cooling cycle, a decreasing trend is observed, with E_{DC} in the range from 1.45-1.15 eV, where the **Cs-dhta** sample shows a minimum. Since the conductivity of the dehydrated samples must primarily rely on through-bond electron transfer, the activation energies will likely depend on the degree of overlap between the metal and ligand orbitals. Therefore, it is unsurprising that the activation energy trends match well with alkali atom size and softness trends, as the softer and larger alkali metals can provide the necessary orbital overlap with ligand oxygen atoms. Generally, E_{DC} values are higher for the cooling cycle, which can be correlated with the decrease of conductivity values in cooling by a few orders of magnitude. The **Na-dhta** and **Cs-dhta** samples display the smallest variation in E_{DC} between cycles before and after transformation, **Table 1**., and at the same time, they are the most sensitive to the loss of ambiental water on the surface, and at the defects and grain boundaries of the sample. All samples are stable after the heating-induced structural transformations, as evidenced by their Arrhenius plots during the cooling cycle (**Fig. 8.a**).

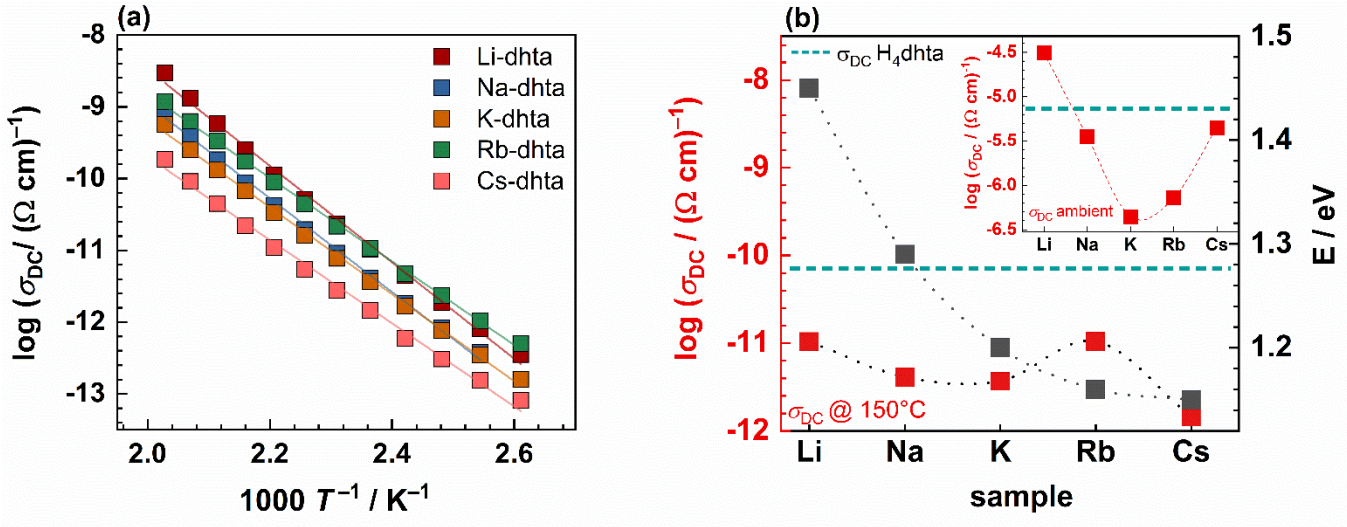

Figure 8 (a) Comparison of Arrhenius plots for the cooling cycle of all **M_{alk}-dhta** materials and (b) comparison of σ_{DC} values for samples measured at ambient conditions (approx. 25 °C and 55% RH) (inset) and the values obtained at 150 °C in a cooling cycle and dry atmosphere (red). The corresponding activation energy values at 150 °C in a dry atmosphere are plotted in dark grey. The teal dashed lines denote the σ_{DC} value for pure H_4**dhta** at ambient conditions (inset) and 150 °C in a cooling cycle and dry atmosphere.

The significantly lower conductivity values after sample dehydration and the related structural changes emphasize the importance of the H-bonding network and active pathways for proton conductivity. Presumably, the main charge carriers in the dehydrated samples are electrons *via* the through-bond mechanism, resulting in a drastically lower overall conductivity (four, three, three, two, and almost five orders of magnitude lower than at ambient conditions for **Li-dhta**, **Na-dhta**, **K-dhta**, **Rb-dhta** and **Cs-dhta**, respectively). The **Cs-dhta** sample, in particular, exhibits a very large shift in DC conductivity, resulting in values comparable to those measured at dry atmospheric conditions (**Fig. S38**). Since both processes seemingly produce **Cs-dhta-anh** (SI 1.4., **Fig. S28**), the similar conductivity of the resulting materials is unsurprising. Unfortunately, despite numerous collection attempts, the PXRD data was not of sufficient quality to solve the structures for other dehydrated **M_{alk}-dhta** phases and to be able to discuss in more detail the structure-conductivity relations after the water loss. The observed trend in DC conductivity after transformation for **M_{alk}-dhta** (M = Li, Na, K, Rb) is similar to the measurements at ambient conditions, except for the aforementioned **Cs-dhta** (compare main **Figure 8b** with Inset).
The DC values obtained for all samples from our study show significantly higher values compared to existing literature data for MOF-74-type frameworks, specifically M_2(**dhta**)$(DMF)_2$ with M = Mg, Mn, Co, Ni, Cu, Zn. The conductivities of these MOF-74-type materials demonstrate orders of magnitude lower values,[27] ranging from $1.4 \cdot 10^{-14}$ $(\Omega\ cm)^{-1}$ to $3.0 \cdot 10^{-13}$ $(\Omega\ cm)^{-1}$ except for the Fe(**dhta**)$(DMF)_2$ sample with $3.2 \cdot 10^{-7}$ $(\Omega\ cm)^{-1}$ conductivity.[29] These frameworks show similar sensitivity to the loss of the crystalline and coordinated solvent as the here-studied **M_{alk}-dhta** samples. The conductivity of the here investigated **M_{alk}-dhta** materials is up to two orders of magnitude higher than even the Li_2-Mn-**dhta** framework ($6.1 \cdot 10^{-7}$ $(\Omega\ cm)^{-1}$) and tetralithium-**dhta** material ($1.1 \cdot 10^{-7}$ $(\Omega\ cm)^{-1}$) tested (as a graphene composite) for high-performing lithium batteries.[33,34] This tetralithium-**dhta** material does not have a reported structure, so it is hard to rationalize the observed difference in performance. The difference is likely due to the presence of coordinated water in the monolithium-**dhta** compound and a well-defined network of hydrogen bonds, resulting in highly proton-conductive **M_{alk}-dhta** materials.

Conclusions

In summary, we have used green and sustainable solvent-free synthetic procedures to efficiently prepare a series of highly conductive (1:1) alkali metal-**dhta** coordination polymers (Li, Na, K, Cs, Rb). Mechanochemical procedures proved advantageous to solution processes, resulting in a high stoichiometric control and a direct and complete conversion to the phase-pure products in minutes without a need for any solvent in the synthesis or work-up. These procedures can be readily scaled to a gram scale using mixer or planetary mill. The structure of the prepared **M_{alk}-dhta** materials is characterized by different alkali-cation polyhedrons, ranging in coordination number from four to ten, depending on the size of the cation and the presence of water. The structure and connectivity of these polyhedrons and the presence of coordinating water molecules are directly related to a non-monotone trend in conductivity, with the K-**dhta** having the lowest DC conductivity in the series and **Li-dhta** the highest. The H_4**dhta** quinone ligand is characterized by a high DC conductivity based on ambient humidity-enhanced proton conductivity and through-space electron transfer stemming from the aromatic core. The tested **M_{alk}-dhta** materials display typical semiconductor behavior expected in such coordination polymers but also some of the highest DC conductivity among reported metal-**dhta** MOFs. Such high conductivity seems to primarily stem from proton transport along the extensive hydrogen bond networks characterizing these materials, which is greatly enhanced by ambient water. In the case of monoalkali **Li-dhta**, the hydrogen-bonded framework is augmented by cocrystallization with fully protonated H_4**dhta** molecules, resulting in orders of magnitude higher conductivity than all the reported **dhta**-based MOF-74 frameworks and even than the tetralithium-**dhta** material tested for lithium-organic batteries application. This result shows how the quantity of metal is not decisive in all cases for the performance of electromaterials, which may have important implications on the economy of precious energy metals, such as lithium. The here-tested materials show colossal changes in conductivity when exposed to dry conditions, making them possibly not suitable for real-world battery applications but good potential candidates for water-sensing. In the future, we will focus on the sustainable preparation and structural characterization of higher stoichiometry **M_{alk}-dhta** samples with lithium and sodium, where we also aim to study the effect of introducing the electron-rich thiol functionalities to the H_4**dhta** ligand to increase conductivity and test their suitability as candidates for alkali metal-ion batteries.

ASSOCIATED CONTENT

Supporting Information

The Supporting Information is available free of charge at https://pubs.acs.org.
Detailed information on all instruments and methods; detailed descriptions of all experiments; full PXRD diffractograms, TGA thermograms, infrared spectra, and other supporting analyses, as well as in-situ PXRD monitoring, Raman, and electrical conductivity measurements. (PDF).

AUTHOR INFORMATION

Corresponding Author

*Ruder Bošković Institute, Bijenička c. 54, 10000 Zagreb, Croatia. E-mail: krunoslav.uzarevic@irb.hr, luka.pavic@irb.hr
Institute of Physics, Bijenička c. 46, 10000 Zagreb, Croatia. E-mail: gzgrablic@ifs.hr.

Author Contributions

TG performed lab synthesis and solved crystal structures from the SCXRD data. **VM** and **BK** performed in situ experiments and collected and analyzed the in situ PXRD data. **TG** and **VM** performed all supporting experiments and analyses (PXRD, IR, TGA) and processed the experimental data. **MR** designed, performed, and, with the support of **LP**, analyzed all of the IS measurements. **IB** and **MA** solved the structures from PXRD data and performed related DFT calculations. **AS** and **GZ** performed Raman measurements and analyzed Raman data. **ME** assisted in using the beamline and integrating collected data. **LP** and **KU** envisioned and supervised the project and acquired funding. **TG**, **MR**, and **VM** drafted the initial manuscript. All authors contributed with valuable discussions and helped to shape the final manuscript. / All authors have given approval to the final version of the manuscript./ ‡These authors contributed equally as co-first authors.

Notes

The spectroscopic, thermal, and impedance spectroscopy data supporting this article have been included as part of the Supplementary Information. The crystallographic data have been deposited with the Cambridge Crystallographic Data Centre (CCDC) under the deposition numbers 2365664-2365669 for the hydrated and 2364123 and 2364124 for the anhydrous compounds. These data can be obtained from the https://www.ccdc.cam.ac.uk/structures/ upon request.

ACKNOWLEDGMENT

The work has been supported in part by the "Research Cooperability" Program of the Croatian Science Foundation from the European Social Fund under the Operational Programme Efficient Human Resources 2014-2020 (grant PZS-2019-02-4129), Croatian Science Foundation (grant IP-2020-02-4702) and NPOO.C3.2.R2-I1.06.0049.

This work was also supported by the project Centre for Advanced Laser Techniques (CALT), co-funded by the European Union through the European Regional Development Fund under the Competitiveness and Cohesion Operational Programme (Grant No. KK.01.1.1.05.0001). We acknowledge DESY (Hamburg, Germany), a member of the Helmholtz Association HGF, for providing experimental facilities. Parts of this research were carried out at PETRA III beamline P02.1. Beamtime was allocated by an In-House contingent. Authors acknowledge the use of SEM Thermo Fisher Scientific model Axia™ ChemiSEM™ at the Ruđer Bošković Institute delivered by the project O-ZIP (Grant Ag. No. KK.01.1.1.11.0001) co-financed by the European Union from the European Regional Development Fund. The authors are pleased to acknowledge Marija Mirosavljević (RBI, Zagreb, Croatia) for recording SEM images.

REFERENCES

(1) Zhou, H.-C. “Joe”; Kitagawa, S. Metal–Organic Frameworks (MOFs). *Chem. Soc. Rev.* **2014**, *43* (16), 5415–5418. https://doi.org/10.1039/C4CS90059F.

(2) Furukawa, H.; Cordova, K. E.; O'Keeffe, M.; Yaghi, O. M. The Chemistry and Applications of Metal-Organic Frameworks. *Science (1979)* **2013**, *341* (6149). https://doi.org/10.1126/science.1230444.

(3) Doustkhah, E.; Hassandoost, R.; Khataee, A.; Luque, R.; Assadi, M. H. N. Hard-Templated Metal–Organic Frameworks for Advanced Applications. *Chem Soc Rev* **2021**, *50* (5), 2927–2953. https://doi.org/10.1039/C9CS00813F.

(4) Bavykina, A.; Kolobov, N.; Khan, I. S.; Bau, J. A.; Ramirez, A.; Gascon, J. Metal–Organic Frameworks in Heterogeneous Catalysis: Recent Progress, New Trends, and Future Perspectives. *Chem Rev* **2020**, *120* (16), 8468–8535. https://doi.org/10.1021/acs.chemrev.9b00685.

(5) Li, X.; Yang, X.; Xue, H.; Pang, H.; Xu, Q. Metal–Organic Frameworks as a Platform for Clean Energy Applications. *EnergyChem* **2020**, *2* (2), 100027. https://doi.org/10.1016/j.enchem.2020.100027.

(6) Mancuso, J. L.; Mroz, A. M.; Le, K. N.; Hendon, C. H. Electronic Structure Modeling of Metal–Organic Frameworks. *Chem Rev* **2020**, *120* (16), 8641–8715. https://doi.org/10.1021/acs.chemrev.0c00148.

(7) Yu, J.; Park, J.; Van Wyk, A.; Rumbles, G.; Deria, P. Excited-State Electronic Properties in Zr-Based Metal–Organic Frameworks as a Function of a Topological Network. *J Am Chem Soc* **2018**, *140* (33), 10488–10496. https://doi.org/10.1021/jacs.8b04980.

(8) Butler, K. T.; Worrall, S. D.; Molloy, C. D.; Hendon, C. H.; Attfield, M. P.; Dryfe, R. A. W.; Walsh, A. Electronic Structure Design for Nanoporous, Electrically Conductive Zeolitic Imidazolate Frameworks. *J Mater Chem C Mater* **2017**, *5* (31), 7726–7731. https://doi.org/10.1039/C7TC03150E.

(9) Li, J.; Wu, R. Metal–Organic Frameworks: Possible New Two-Dimensional Magnetic and Topological Materials. *Nanoscale* **2020**, *12* (46), 23620–23625. https://doi.org/10.1039/D0NR05748G.

(10) Liu, H.; Wang, Y.; Qin, Z.; Liu, D.; Xu, H.; Dong, H.; Hu, W. Electrically Conductive Coordination Polymers for Electronic and Optoelectronic Device Applications. *J Phys Chem Lett* **2021**, *12* (6), 1612–1630. https://doi.org/10.1021/acs.jpclett.0c02988.

(11) Lin, L.; Zhang, Q.; Ni, Y.; Shang, L.; Zhang, X.; Yan, Z.; Zhao, Q.; Chen, J. Rational Design and Synthesis of Two-Dimensional Conjugated Metal-Organic Polymers for Electrocatalysis Applications. *Chem* **2022**, *8* (7), 1822–1854. https://doi.org/10.1016/j.chempr.2022.03.027.

(12) Wang, S.; Liu, J.; Zhao, H.; Guo, Z.; Xing, H.; Gao, Y. Electrically Conductive Coordination Polymer for Highly Selective Chemiresistive Sensing of Volatile Amines. *Inorg Chem* **2018**, *57* (2), 541–544. https://doi.org/10.1021/acs.inorgchem.7b02464.

(13) Park, C.; Baek, J. W.; Shin, E.; Kim, I.-D. Two-Dimensional Electrically Conductive Metal–Organic Frameworks as Chemiresistive Sensors. *ACS Nanoscience Au* **2023**, *3* (5), 353–374. https://doi.org/10.1021/acsnanoscienceau.3c00024.

(14) Wang, J.; Guo, X.; Apostol, P.; Liu, X.; Robeyns, K.; Gence, L.; Morari, C.; Gohy, J.-F.; Vlad, A. High Performance Li-, Na-, and K-Ion Storage in Electrically Conducting Coordination Polymers. *Energy Environ Sci* **2022**, *15* (9), 3923–3932. https://doi.org/10.1039/D2EE00566B.

(15) Liu, J.; Zheng, M.; Wu, S.; Zhang, L. Design Strategies for Coordination Polymers as Electrodes and Electrolytes in Rechargeable Lithium Batteries. *Coord Chem Rev* **2023**, *483*, 215084. https://doi.org/10.1016/j.ccr.2023.215084.

(16) Xie, L. S.; Skorupskii, G.; Dincă, M. Electrically Conductive Metal–Organic Frameworks. *Chem Rev* **2020**, *120* (16), 8536–8580. https://doi.org/10.1021/acs.chemrev.9b00766.

(17) Nath, A.; Asha, K. S.; Mandal, S. Conductive Metal-Organic Frameworks: Electronic Structure and Electrochemical Applications. *Chemistry – A European Journal* **2021**, *27* (45), 11482–11538. https://doi.org/10.1002/chem.202100610.

(18) Sun, L.; Campbell, M. G.; Dincă, M. Electrically Conductive Porous Metal–Organic Frameworks. *Angewandte Chemie International Edition* **2016**, *55* (11), 3566–3579. https://doi.org/10.1002/anie.201506219.

(19) Rosi, N. L.; Kim, J.; Eddaoudi, M.; Chen, B.; O'Keeffe, M.; Yaghi, O. M. Rod Packings and Metal−Organic Frameworks Constructed from Rod-Shaped Secondary Building Units. *J Am Chem Soc* **2005**, *127* (5), 1504–1518. https://doi.org/10.1021/ja045123o.

(20) Furukawa, H.; Cordova, K. E.; O'Keeffe, M.; Yaghi, O. M. The Chemistry and Applications of Metal-Organic Frameworks. *Science (1979)* **2013**, *341* (6149). https://doi.org/10.1126/science.1230444.

(21) Zhang, Q.; Li, B.; Chen, L. First-Principles Study of Microporous Magnets M-MOF-74 (M = Ni, Co, Fe, Mn): The Role of Metal Centers. *Inorg Chem* **2013**, *52* (16), 9356–9362. https://doi.org/10.1021/ic400927m.

(22) Mukoyoshi, M.; Maesato, M.; Kawaguchi, S.; Kubota, Y.; Cho, K.; Kitagawa, Y.; Kitagawa, H. Systematic Tuning of the Magnetic Properties in Mixed-Metal MOF-74. *Inorg Chem* **2022**, *61* (19), 7226–7230. https://doi.org/10.1021/acs.inorgchem.2c00646.

(23) Flores, J. G.; Díaz-García, M.; Ibarra, I. A.; Aguilar-Pliego, J.; Sánchez-Sánchez, M. Sustainable M-MOF-74 (M = Cu, Co, Zn) Prepared in Methanol as Heterogeneous Catalysts in the Synthesis of Benzaldehyde from Styrene Oxidation. *J Solid State Chem* **2021**, *298*, 122151. https://doi.org/10.1016/j.jssc.2021.122151.

(24) Ayoub, G.; Karadeniz, B.; Howarth, A. J.; Farha, O. K.; Đilović, I.; Germann, L. S.; Dinnebier, R. E.; Užarević, K.; Friščić, T. Rational Synthesis of Mixed-Metal Microporous Metal–Organic Frameworks with Controlled Composition Using Mechanochemistry. *Chemistry of Materials* **2019**, *31* (15), 5494–5501. https://doi.org/10.1021/acs.chemmater.9b01068.

(25) Muratović, S.; Martinez, V.; Karadeniz, B.; Pajić, D.; Brekalo, I.; Arhangelskis, M.; Mazaj, M.; Mali, G.; Etter, M.; Friščić, T.; Krupskaya, Y.; Kataev, V.; Žilić, D.; Užarević, K. Low-Dimensional Magnetism in Multivariate Copper/Zinc MOF-74 Materials Formed via Different Mechanochemical Methods. *Inorg Chem* **2022**, *61* (45), 18181–18192. https://doi.org/10.1021/acs.inorgchem.2c02898.

(26) Do, J.-L.; Friščić, T. Chemistry 2.0: Developing a New, Solvent-Free System of Chemical Synthesis Based on Mechanochemistry. *Synlett* **2017**, *28* (16), 2066–2092. https://doi.org/10.1055/s-0036-1590854.

(27) Sun, L.; Hendon, C. H.; Park, S. S.; Tulchinsky, Y.; Wan, R.; Wang, F.; Walsh, A.; Dincă, M. Is Iron Unique in Promoting Electrical Conductivity in MOFs? *Chem Sci* **2017**, *8* (6), 4450–4457. https://doi.org/10.1039/C7SC00647K.

(28) Sun, L.; Miyakai, T.; Seki, S.; Dincă, M. Mn_2 (2,5-Disulfhydrylbenzene-1,4-Dicarboxylate): A Microporous Metal–Organic Framework with Infinite $(-Mn-S-)_\infty$ Chains and High Intrinsic Charge Mobility. *J Am Chem Soc* **2013**, *135* (22), 8185–8188. https://doi.org/10.1021/ja4037516.

(29) Sun, L.; Hendon, C. H.; Minier, M. A.; Walsh, A.; Dincă, M. Million-Fold Electrical Conductivity Enhancement in Fe_2 (DEBDC) versus Mn_2 (DEBDC) (E = S, O). *J Am Chem Soc* **2015**, *137* (19), 6164–6167. https://doi.org/10.1021/jacs.5b02897.

(30) Lupa, M.; Kozyra, P.; Jajko, G.; Matoga, D. Trojan Horse Thiocyanate: Induction and Control of High Proton Conductivity in CPO-27/MOF-74 Metal–Organic Frameworks by Metal Selection and Solvent-Free Mechanochemical Dosing. *ACS Appl Mater Interfaces* **2021**, *13* (25), 29820–29826. https://doi.org/10.1021/acsami.1c06346.

(31) Lupa, M.; Kozyra, P.; Matoga, D. Solvent-Free Mechanochemical Dense Pore Filling Yields CPO-27/MOF-74 Metal–Organic Frameworks with High Anhydrous and Water-Assisted Proton Conductivity. *ACS Appl Energy Mater* **2023**, *6* (18), 9118–9123. https://doi.org/10.1021/acsaem.2c03518.

(32) Rambabu, D.; Lakraychi, A. E.; Wang, J.; Sieuw, L.; Gupta, D.; Apostol, P.; Chanteux, G.; Goossens, T.; Robeyns, K.; Vlad, A. An Electrically Conducting Li-Ion Metal–Organic Framework. *J Am Chem Soc* **2021**, *143* (30), 11641–11650. https://doi.org/10.1021/jacs.1c04591.

(33) Zhao, Q.; Wang, J.; Chen, C.; Ma, T.; Chen, J. Nanostructured Organic Electrode Materials Grown on Graphene with Covalent-Bond Interaction for High-Rate and Ultra-Long-Life Lithium-Ion Batteries. *Nano Res* **2017**, *10* (12), 4245–4255. https://doi.org/10.1007/s12274-017-1580-9.

(34) Wang, S.; Wang, L.; Zhang, K.; Zhu, Z.; Tao, Z.; Chen, J. Organic $Li_4C_8H_2O_6$ Nanosheets for Lithium-Ion Batteries. *Nano Lett* **2013**, *13* (9), 4404–4409. https://doi.org/10.1021/nl402239p.

(35) Quarez, É.; Jouhara, A.; Grolleau, S.; Dolhem, F.; Dupré, N.; Poizot, P. From Partial to Complete Neutralization of 2,5-Dihydroxyterephthalic Acid in the Li–Na System: Crystal Chemistry and Electrochemical Behavior of $Na_2Li_2C_8H_2O_6$ *vs.* Li. *CrystEngComm* **2020**, *22* (9), 1653–1663. https://doi.org/10.1039/C9CE01674K.

(36) Halasz, I.; Kimber, S. A. J.; Beldon, P. J.; Belenguer, A. M.; Adams, F.; Honkimäki, V.; Nightingale, R. C.; Dinnebier, R. E.; Friščić, T. In Situ and Real-Time Monitoring of Mechanochemical Milling Reactions Using Synchrotron X-Ray Diffraction. *Nat Protoc* **2013**, *8* (9), 1718–1729. https://doi.org/10.1038/nprot.2013.100.

(37) Butler, K. T.; Worrall, S. D.; Molloy, C. D.; Hendon, C. H.; Attfield, M. P.; Dryfe, R. A. W.; Walsh, A. Electronic Structure Design for Nanoporous, Electrically Conductive Zeolitic Imidazolate Frameworks. *J Mater Chem C Mater* **2017**, *5* (31), 7726–7731. https://doi.org/10.1039/C7TC03150E.

(38) Cliffe, M. J.; Mottillo, C.; Stein, R. S.; Bučar, D.-K.; Friščić, T. Accelerated Aging: A Low Energy, Solvent-Free Alternative to Solvothermal and Mechanochemical Synthesis of Metal–Organic Materials. *Chem Sci* **2012**, *3* (8), 2495–2500. https://doi.org/10.1039/C2SC20344H.

(39) Groom, C. R.; Bruno, I. J.; Lightfoot, M. P.; Ward, S. C. The Cambridge Structural Database. *Acta Crystallogr B Struct Sci Cryst Eng Mater* **2016**, *72* (2), 171–179. https://doi.org/10.1107/S2052520616003954.

(40) Starodubtseva, A. A.; Dubrovskiy, V. A.; Malik, S. D.; Lyssenko, K. A.; Sembayeva, A. M.; Morontsev, A. A.; Galeyeva, A. K.; Trussov, I. A. Some Aspects of MOF-74 (Zn $_2$ DOBDC) Metal–Organic Framework Formation Using THF as the Solvent. *CrystEngComm* **2024**, *26* (43), 6161–6171. https://doi.org/10.1039/D4CE00905C.

(41) Hadjiivanov, K. I.; Panayotov, D. A.; Mihaylov, M. Y.; Ivanova, E. Z.; Chakarova, K. K.; Andonova, S. M.; Drenchev, N. L. Power of Infrared and Raman Spectroscopies to Characterize Metal- Organic Frameworks and Investigate Their Interaction with Guest Molecules. **2021**. https://doi.org/10.1021/acs.chemrev.0c00487.

(42) Ryder, M. R.; Civalleri, B.; Cinque, G.; Tan, J. C. Discovering Connections between Terahertz Vibrations and Elasticity Underpinning the Collective Dynamics of the HKUST-1 Metal-Organic Framework. *CrystEngComm* **2016**, *18* (23), 4303–4312. https://doi.org/10.1039/c5ce02347e.

(43) Ryder, M. R.; Civalleri, B.; Bennett, T.; Henke, S.; Rudić, S.; Cinque, G.; Fernandez-Alonso, F.; Tan, J. C. Identifying the Role of Terahertz Vibrations in Metal-Organic Frameworks: From Gate-Opening Phenomenon to Shear-Driven Structural Destabilization. *Phys Rev Lett* **2014**, *113* (21), 1–6. https://doi.org/10.1103/PhysRevLett.113.215502.

(44) Möslein, A. F.; Tan, J. C. Vibrational Modes and Terahertz Phenomena of the Large-Cage Zeolitic Imidazolate Framework-71. *Journal of Physical Chemistry Letters* **2022**, *13* (12), 2838–2844. https://doi.org/10.1021/acs.jpclett.2c00081.

(45) Formalik, F.; Fischer, M.; Kuchta, B. Correlating Phonons and Deformations: A Method for Structural Phase Transformation Analysis in Metal-Organic Frameworks. *Cryst Growth Des* **2023**, *23* (12), 8962–8971. https://doi.org/10.1021/acs.cgd.3c01013.

(46) Qian, X.; Zhou, J.; Chen, G. Phonon-Engineered Extreme Thermal Conductivity Materials. *Nat Mater* **2021**, *20* (9), 1188–1202. https://doi.org/10.1038/s41563-021-00918-3.

(47) Ying, P.; Zhang, J.; Zhong, Z. Effect of Phase Transition on the Thermal Transport in Isoreticular DUT Materials. *Journal of Physical Chemistry C* **2021**, *125* (23), 12991–13001. https://doi.org/10.1021/acs.jpcc.1c02767.

(48) Tan, K.; Zuluaga, S.; Gong, Q.; Canepa, P.; Wang, H.; Li, J.; Chabal, Y. J.; Thonhauser, T. Water Reaction Mechanism in Metal Organic Frameworks with Coordinatively Unsaturated Metal Ions: MOF-74. *Chemistry of Materials* **2014**, *26* (23), 6886–6895. https://doi.org/10.1021/cm5038183.

(49) Strauss, I.; Mundstock, A.; Hinrichs, D.; Himstedt, R.; Knebel, A.; Reinhardt, C.; Dorfs, D.; Caro, J. The Interaction of Guest Molecules with Co-MOF-74: A Vis/NIR and Raman Approach. *Angewandte Chemie - International Edition* **2018**, *57* (25), 7434–7439. https://doi.org/10.1002/anie.201801966.

(50) Strauss, I.; Mundstock, A.; Treger, M.; Lange, K.; Hwang, S.; Chmelik, C.; Rusch, P.; Bigall, N. C.; Pichler, T.; Shiozawa, H.; Caro, J. Metal-Organic Framework Co-MOF-74-Based Host-Guest Composites for Resistive Gas Sensing. *ACS Appl Mater Interfaces* **2019**, *11* (15), 14175–14181. https://doi.org/10.1021/acsami.8b22002.

(51) Beard, M. C.; Turner, G. M.; Schmuttenmaer, C. A. Terahertz Spectroscopy. *J Phys Chem B* **2002**, *106* (29), 7146–7159. https://doi.org/10.1021/jp020579i.

(52) Neu, J.; Nikonow, H.; Schmuttenmaer, C. A. Terahertz Spectroscopy and Density Functional Theory Calculations of <scp>dl</Scp> -Norleucine and <scp>dl</Scp> -Methionine. *J Phys Chem A* **2018**, *122* (28), 5978–5982. https://doi.org/10.1021/acs.jpca.8b04978.

(53) Formalik, F.; Fischer, M.; Kuchta, B. Correlating Phonons and Deformations: A Method for Structural Phase Transformation Analysis in Metal–Organic Frameworks. *Cryst Growth Des* **2023**, *23* (12), 8962–8971. https://doi.org/10.1021/acs.cgd.3c01013.

(54) Pili, S.; Rought, P.; Kolokolov, D. I.; Lin, L.; da Silva, I.; Cheng, Y.; Marsh, C.; Silverwood, I. P.; García Sakai, V.; Li, M.; Titman, J. J.; Knight, L.; Daemen, L. L.; Ramirez-Cuesta, A. J.; Tang, C. C.; Stepanov, A. G.; Yang, S.; Schröder, M. Enhancement of Proton Conductivity in Nonporous Metal–Organic Frameworks: The Role of Framework Proton Density and Humidity. *Chemistry of Materials* **2018**, *30* (21), 7593–7602. https://doi.org/10.1021/acs.chemmater.8b02765.

(55) Lozančić, A.; Burazer, S.; Renka, S.; Molčanov, K.; Molčanov, L.; Jurić, M. Proton Transport in Oxalate Compounds of Iron(<scp>iii</Scp>) Containing (Alkyl)Ammonium Cations: The Influence of the Density of Hydrogen Bonds on Conductivity. *CrystEngComm* **2024**, *26* (13), 1892–1901. https://doi.org/10.1039/D3CE01267K.

(56) Nguyen, M. V.; Dong, H. C.; Nguyen-Manh, D.; Vu, N. H.; Trinh, T. T.; Phan, T. B. Effect of Hydrogen-Bonding Networks in Water on the Proton Conductivity Properties of Metal–Organic Frameworks. *Journal of Science: Advanced Materials and Devices* **2021**, *6* (4), 509–515. https://doi.org/10.1016/j.jsamd.2021.06.005.

(57) Xiang, F.; Chen, S.; Yuan, Z.; Li, L.; Fan, Z.; Yao, Z.; Liu, C.; Xiang, S.; Zhang, Z. Switched Proton Conduction in Metal–Organic Frameworks. *JACS Au* **2022**, *2* (5), 1043–1053. https://doi.org/10.1021/jacsau.2c00069.

(58) Lupa-Myszkowska, M.; Oszajca, M.; Matoga, D. From Non-Conductive MOF to Proton-Conducting Metal-HOFs: A New Class of Reversible Transformations Induced by Solvent-Free Mechanochemistry. *Chem Sci* **2023**, *14* (48), 14176–14181. https://doi.org/10.1039/D3SC04401G.

(59) Xie, X.-X.; Yang, Y.-C.; Dou, B.-H.; Li, Z.-F.; Li, G. Proton Conductive Carboxylate-Based Metal–Organic Frameworks. *Coord Chem Rev* **2020**, *403*, 213100. https://doi.org/10.1016/j.ccr.2019.213100.

(60) Lozančić, A.; Burazer, S.; Šenjug, P.; Renka, S.; Molčanov, K.; Pajić, D.; Dubraja, L. A.; Jurić, M. Facile One-Step Preparation of Co2CrO4 Spinel from Heterometallic Compounds – Structural, Magnetic, Electrical and Photocatalytic Studies. *J Alloys Compd* **2024**, *986*, 174087. https://doi.org/10.1016/j.jallcom.2024.174087.